Clays and Clay Minerals, Vol. 47, No. 3, 252–268, 1999.

Mg-SMECTITE AUTHIGENESIS IN A MARINE EVAPORATIVE ENVIRONMENT, SALINA OMETEPEC, BAJA CALIFORNIA

VICTORIA C. HOVER,† LYNN M. WALTER, DONALD R. PEACOR, AND ANNA M. MARTINI

Department of Geological Sciences, University of Michigan, 2534 C. C. Little Building, 425 E. University, Ann Arbor, Michigan 48109-1063, USA

Abstract—Formation of authigenic trioctahedral Mg-rich smectite is common in evaporative lake sediments, but was not described previously in modern marine evaporative environments. This study documents formation of authigenic K-rich, Mg-smectite during very early diagenesis in the dominantly siliciclastic Salina Ometepec (Baja California), a large supratidal evaporative sabkha complex near the mouth of the Colorado River. Here, sediment pore waters are exceptionally Mg^{2+}-rich relative to other marine evaporative environments due to suppressed sulfate reduction which limits production of carbonate alkalinity and, hence, carbonate (particularly dolomite) precipitation. Sediment cores were obtained along a five km transect seaward across the hypersaline mud flat to evaluate how these atypical geochemical conditions would affect the clay mineral compositions.

Scanning transmission electron microscopy (STEM) observations show that the smectite from the marine Inlet, near the sediment source, consists of grains of irregular shape that give selected area diffraction (SAED) patterns reflecting dominant turbostratic stacking. Analytical electron microscopy (AEM) analyses indicate that K^+ is the dominant interlayer cation; the mean composition is approximately $K_{0.7}(Al_{3.3}Fe(III)_{0.3}Mg_{0.5})(Al_{0.5}Si_{7.5})O_{20}(OH)_4$. Such smectite is implied to be detrital in part because it is similar to smectite known to be deposited by the Colorado River.

Smectite from the hypersaline mud flat occurs as aggregates of small subhedral pseudohexagonal plate or lath-shaped crystals ≤250 nm in diameter, with thicknesses varying between three and ten layers. The SAED patterns reflect substantial turbostratic stacking, but with a greater frequency of interlayer coherency as compared with detrital smectite. Crystals from greater sediment depths are larger and more nearly euhedral. This smectite is dominantly trioctahedral, with mean composition approximately $K_{0.7}(Al_{0.7}Fe(III)_{0.5}Mg_{4.45})(Al_{1.2}Si_{6.8})O_{20}(OH)_4$ (saponitic). This smectite is inferred to be dominantly authigenic in origin.

The X-ray diffraction (XRD) and STEM/AEM data collectively imply that detrital aluminous dioctahedral smectite reacts to form authigenic Mg-rich trioctahedral smectite, driven in part by the high Mg^{2+}/Ca^{2+} ratio of pore waters. Such early-formed Mg-rich smectite may be the precursor for the trioctahedral mixed-layer smectite, corrensite, and chlorite assemblages found in ancient marine evaporative sequences. These results also add to the accumulating evidence that interlayer K^+ in marine smectite is fixed during the earliest stages of marine diagenesis near the sediment water interface.

Key Words—Baja California, Early Diagenesis, Hypersaline Brines, K-smectite, Mg-smectite, Salina Ometepec, Saponite, Trioctahedral Smectite.

INTRODUCTION

Studies of modern hypersaline alkaline lacustrine or playa environments in arid continental settings show that the compositions of smectite-like clay minerals may be modified by interactions with chemically-evolved brines. (*e.g.*, Tardy *et al.*, 1974; Gac *et al.*, 1977; Ataman and Baysal, 1978; Stoffers and Singer, 1979; Singer and Stoffers, 1980; Jones and Weir, 1983; Jones and Spencer, 1985). Hypersaline lake and sediment pore waters commonly have relatively high pH values (7–10) and high Na^+, HCO_3^-, and CO_3^{2-} concentrations (*e.g.*, Eugster and Hardie, 1978; Eugster and Jones, 1979). The TEM and AEM study of authigenesis in the alkaline playa Lake Abert (Oregon) by Banfield *et al.* (1991a, 1991b) showed that Mg-rich trioctahedral smectite similar to stevensite in composition (Brindley, 1955), with K^+ as the dominant interlayer cation, formed as an overgrowth on and/or alteration product of original detrital aluminous dioctahedral smectite. Surface lake waters became depleted in K^+, Mg^{2+}, and H_4SiO_4 relative to other conservative elements concurrent with Mg-smectite authigenesis (Jones and Weir, 1983, and references therein).

Such modern lacustrine hypersaline geochemical environments provide analogs for ancient lacustrine sediments in which Mg-rich trioctahedral mixed-layer illite-smectite, corrensite, and chlorite assemblages form during subsequent burial diagenesis, as in the Green River Formation (*e.g.*, Dyni, 1976; Tettenhorst and Moore, 1978) and other formations (*e.g.*, Turner and Fishman, 1991; Hillier, 1993). However, trioctahedral Mg-rich clay associations were reported from hypersaline marine environments such as the Silurian-age sediments in the Appalachian Basin, New York (Bodine and Standaert, 1977; Bodine, 1985), the Pennsylvanian-age sediments in the Paradox Basin, Utah

† Present Address: Department of Geological Sciences, Rutgers/Newark, 407 Boyden Hall, 195 University Ave., Newark, New Jersey 07102, USA.

(Bodine and Madsen, 1987), and the Permian-age sediments, west Texas (Fisher, 1988; Andreason, 1992). Evaporative marine depositional environments differ significantly from lacustrine settings in having pH values (7–8) and solute concentrations controlled primarily by the extent of seawater evaporation (*e.g.*, Carpenter, 1978; Holser, 1979). The formation of Mg-rich smectite in modern marine sediments was described for marine shelf environments (Drever, 1971), but no studies of clay mineralogy and chemistry in modern marine hypersaline sabkha environments are available.

The hypersaline, supratidal sabkha complex of the Salina Ometepec, along the northwest margin of the Gulf of California (Sea of Cortez), Mexico, provides an excellent modern laboratory for observing the potential interaction of marine brines with the rapidly deposited clay-rich sediments supplied by the Colorado River. The mass-balance considerations of Na^+-Cl^--Br^- of these Salina Ometepec surface and pore water brines indicates that salinity is derived largely from the evaporation of seawater to the point of halite saturation. Selective dissolution and recycling of previously precipitated, late-stage evaporite minerals can occur near the sediment-water interface (*e.g.*, sylvite (KCl), carnalite ($KMgCl_3 \cdot 6H_2O$), bishoffite ($MgCl_2 \cdot 6H_2O$), and kieserite ($MgSO_4 \cdot H_2O$)). This process can contribute excess Mg^{2+}, K^+ and Br^- to the overlying surface water relative to concentrations expected for evaporation alone (Martini and Walter, 1993; Martini, 1997).

The extreme salinity and temperature fluctuations at the Salina Ometepec severely limit the organic matter supply to these sediments and inhibit microbial sulfate reduction and production of carbonate alkalinity in the pore waters (Hansen *et al.*, 1993; Martini and Walter, 1993). Lack of sulfate reduction in Salina sediments contrasts with normal marine siliciclastic environments, where sulfate reduction via microbial oxidation of organic matter is common and the generation of HCO_3^- and H_2S in pore waters promotes the formation of authigenic Ca-, Mg- and Fe-carbonates and Fe-sulfides (*e.g.*, Berner, 1984). Lack of HCO_3^- generation in the largely "aseptic" Salina Ometepec sediments prevents significant removal of Ca^{2+} and Mg^{2+} by calcite and dolomite mineral precipitation, and results in more elevated Mg^{2+}/Ca^{2+} ratios and higher Mg^{2+} concentrations in pore waters than are typically observed in carbonate-dominated sabkhas (*e.g.*, Butler, 1969).

The goal of the present study was to determine whether the unusually Mg^{2+}- and K^+-rich nature of the hypersaline waters in the Salina Ometepec sabkha complex would promote either early Mg^{2+} and K^+ fixation in detrital smectite or neoformation of Mg^{2+}- and K^+-rich smectite-like clay minerals during early diagenesis. The textural, compositional, and structural characteristics of smectite from the hypersaline sabkha sediments, as determined by XRD, STEM, and AEM methods, were compared to the characteristics of smectite from the adjacent normal salinity (marine) Gulf of California sediments to determine how the evolution of pore water compositions during evaporation affected the early elemental fixation of Mg^{2+} and K^+ in the clays.

PHYSICAL AND HYDROGEOCHEMICAL FRAMEWORK OF THE SALINA OMETEPEC

The Salina Ometepec is part of a large (~100 × 20 km) coastal hypersaline, supratidal, sabkha complex that borders the northwestern Gulf of California near the mouth of the Colorado River (Figure 1). The complex lies in a tectonically active region including the San Andreas strike-slip and Gulf of California extensional fault systems (Larson *et al.*, 1968; Humphreys and Weldon, 1991; Suarez-Vidal *et al.*, 1991; Ortlieb, 1991). The coastal mud flat complex is flanked on the west by the San Felipe Mountains (Thompson, 1968) composed of medium-K to high (1–4 wt. %) calc-alkaline andesite with lesser amounts of dacite, basalt, and rhyolite volcanics of Miocene to Pliocene age (Sawlan, 1991). The mountains are bounded on the east by the El Chinero fault, which extends northward from El Chinero and is part of the Main Gulf Escarpment fault system (Suarez-Vidal *et al.*, 1991). This active fault separates the Pliocene- to Pleistocene-age alluvial fans, containing detritus shed from the mountains, from the subsiding Holocene-age coastal mud flat deposits associated with the mouth of the Colorado River (Suarez-Vidal *et al.*, 1991).

The supratidal environment is ~3–5 m above mean sea level (Thompson, 1968) and is flooded intermittently by seawater from both high spring tides and local storms (Vonder Haar and Gorsline, 1975). Because of warm temperatures (mean annual, 18°C; summer, 38–45°C), low annual rainfall (<8 cm y^{-1}), and high evaporation rates (~290 cm y^{-1}) (Thompson, 1968), the supratidal environment is characterized by an evaporative sabkha system including a salina occupying a slight depression near the landward margin of the sabkha and hypersaline mud flats (Thompson, 1968; Kinsman, 1969; Shearman, 1970; Seidell, 1984) (Figure 1). The sabkha complex is recharged with Gulf of California seawater during flooding from the south at the Inlet (Figure 1).

The silt and mud-rich sediments comprising the supratidal mud flat are derived primarily from the suspended load of the Colorado River (Thompson, 1968; Walker and Thompson, 1968), which is composed of subequal amounts of dioctahedral smectite (montmorillonite), illite, and kaolinite (Grim *et al.*, 1949; Thompson, 1968). Provenance studies of the sand-sized grains consisting of quartz, K-feldspar, plagioclase feldspar, illite and/or muscovite, and chlorite, (Thompson, 1968) also indicate a source predominantly from the Colorado River (Merriam and Bandy, 1965; Thompson, 1968). The persistence of clay, silt,

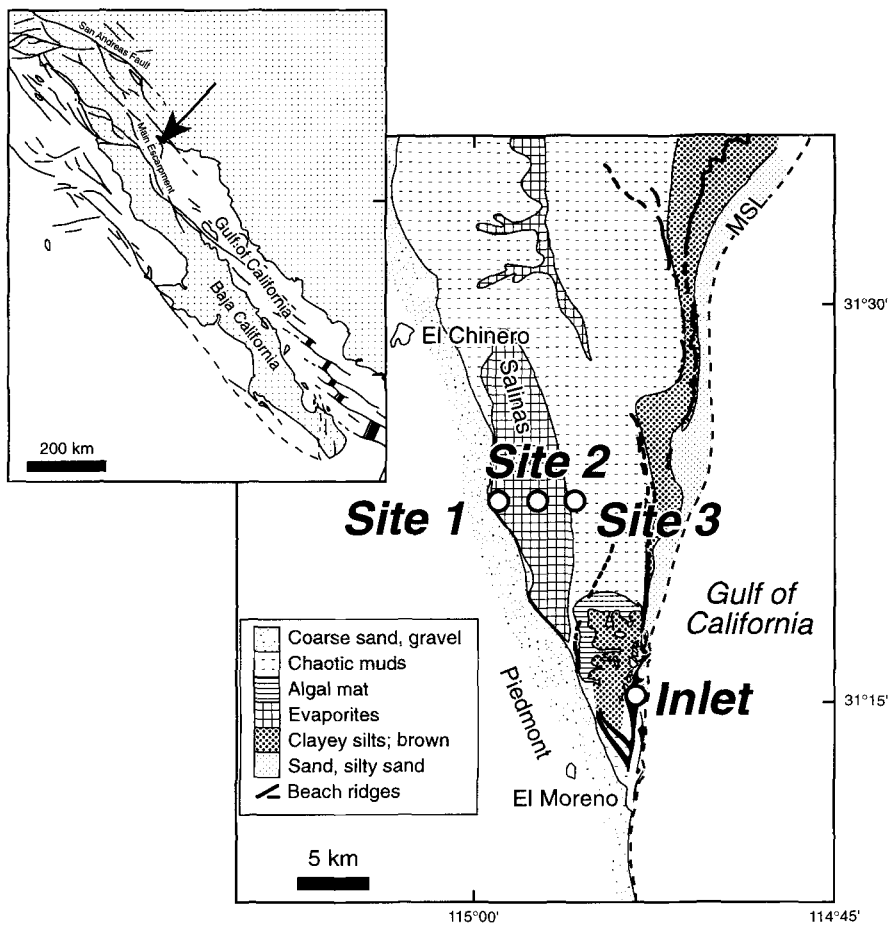

Figure 1. Map showing location of sampling sites and surficial sediment lithologies in the Salina Ometepec, Baja California (after Thompson, 1968; Ortlieb, 1991). The dashed line refers to mean sea level (MSL).

and sand accumulation in the sabkha with Colorado River suspended and bed load mineralogies suggesting that much of the sediment may be remobilized from offshore subtidal sediments (Thompson, 1968). A linear sedimentation rate of ~11 cm y^{-1} was determined from excess ^{210}Pb data for the top 15 cm of sabkha sediments (Martini, 1997). This rate suggests reworking of previously sediments as the dominant depositional process. Current Colorado River discharge volumes have declined over 96% since completion of the Hoover Dam (Baba *et al.*, 1991a, 1991b), and could not support this sedimentation rate.

Outwash from the alluvial fans associated with the San Felipe mountains contributes some predominantly sand-sized material composed of K-feldspar, plagioclase feldspar, biotite, volcanic glass, and rock fragments (Thompson, 1968) along a thin belt on the western margin of the mud-flat (Figure 1). The proportion of clay-sized material in these deposits is small (Thompson, 1968; Seidell, 1984). Occasional, heavy rains may transport some of this material into the salina and mud flat. Aeolian deposition of fine silt- and clay-sized particle derived from weathering and erosion of alluvial fan material (especially micas) on the mud flat also occurs (Seidell, 1984).

During closed-system evaporation of seawater (*e.g.*, no sediment-brine interaction), Br^- commonly behaves as a conservative element whose concentration depends only on the extent of evaporation (*e.g.*, Carpenter, 1978; Holser, 1979; McCaffrey *et al.*, 1987). Martini and Walter (1993) evaluated sediment-pore water interactions in the Salina Ometepec hypersaline sabkha mud flat by considering deviations of element/Br^- ratios relative to established trends for conservative behavior. The Na^+-Cl^--Br^- systematics of Salina surface waters are consistent with evaporation of seawater to the point of halite saturation, modified by the dissolution of previously deposited halite crusts during flooding of the sabkha mud flat by more dilute seawater (Martini and Walter, 1993; Martini, 1997). However, the composition of sediment pore waters also reflects the selective dissolution of Br^--rich late-stage K^+- and Mg^{2+}-chloride salts such as sylvite or carnalite (Martini, 1997). The dissolution of these more sol-

https://doi.org/10.1346/CCMN.1999.0470302 Published online by Cambridge University Press

Table 1. Representative surface and pore water compositions.

Sample	Concentrations in mM[1]								Mole ratios		
	Na^+	Mg^{2+}	Ca^{2+}	K^+	Cl^-	Br^-	SO_4^{2-}	Alk.	Mg:Ca	$Mg:SO_4$	$Ca:SO_4$
Standard seawater	480	54.0	10.5	10.4	558	0.859	28.9	2.37	4.69	1.87	0.364
Gulf of California seawater	505	57.1	11.2	12.7	582	0.904	28.8	2.48	5.12	1.98	0.397
Site 1 Surface water	2380	175	38.8	53.4	2650	3.08	89.4	3.60	4.50	1.95	0.434
Site 1 Pore water, 42–43 cm	2920	344	23.6	100	3310	6.28	98.9	3.78	14.6	3.48	0.238
Site 3 Surface water	2880	232	34.8	45.5	3210	3.88	101	3.68	6.68	2.30	0.344
Site 3 Pore water, 42–43 cm	3190	457	19.4	120	3940	8.66	128	n.d.	23.6	3.57	0.151

[1] Seawater concentrations from Millero (1974); all others from Martini (1997); mM = milli-mole/liter. Alk. = total alkalinity as HCO_3^-. n.d. = not determined.

uble late-stage chloride minerals increases the Br^-, Mg^{2+}, and K^+ concentrations in pore waters relative to conservative evaporation trends and makes Br^- concentrations a less reliable index of degree of evaporative concentration.

Unlike organic-rich hypersaline sediment systems where microbial SO_4^{2-} reduction produces alkalinity, there is little SO_4^{2-} reduction and HCO_3^- production in low organic-carbon Salina Ometepec sediment pore waters. Here, SO_4^{2-} and Ca^{2+} concentrations of pore waters are controlled solely by gypsum precipitation. As a result, these species follow a predictable trend with seawater evaporation and so permit better estimation of the extent of evaporation than does Br^- (Martini, 1997). Even though the Mg^{2+}/Ca^{2+} ratio of Salina pore waters is high, the lack of organic matter and absence of significant HCO_3^- production severely suppresses dolomite precipitation. Thus, the Salina Ometepec pore waters are enriched in Mg^{2+} as a result of the combined effect of lack of dolomite precipitation and Mg-salt dissolution.

In addition to excess K^+ in Salina Ometepec pore waters derived from the selective dissolution of authigenic K^+-chloride salts, dissolution of detrital K-feldspar, biotite and illite-muscovite also contribute to elevated K^+ concentrations in sediment pore waters (Hansen *et al.*, 1993; Martini and Walter, 1993; Martini, 1997).

MATERIALS AND ANALYTICAL METHODS

Sediments, pore waters, and surface water samples were obtained from three sites along a five km transect across the Salina Ometepec in February 1993 in connection with the geochemical study of the sabkha complex (Figure 1) (Hansen *et al.*, 1993; Martini and Walter, 1993; Martini, 1997). Site 1 is the westernmost (landward) site and occurs within the salina itself. Site 2 and Site 3 in the supratidal mud flat, are ~2.5 and 5 km to the east of Site 1, respectively. Surface waters and interstitial pore waters were collected at each site to a maximum depth of 1 m via peepers and peizometers implanted in the sediment (Martini and Walter, 1993; Martini, 1997). Data are available for overlying and pore waters including pH, Cl^-, Br^-, SO_4^{2-}, Na^+, Ca^{2+}, Mg^{2+}, K^+, Sr^{2+}, Li^+, Ba^{2+}, H_4SiO_4, $B(OH)_4^-$, Fe^{3+}, Mn^{2+}, and Zn^{2+} (Martini, 1997). The discussion of these data focuses on the relationship between pore water composition and the formation of authigenic clay minerals in the sediment. Table 1 reports representative compositions of the Gulf of California surface water at the Inlet and hypersaline surface and sediment pore waters from the most landward Site 1 and most seaward Site 3 in the mud flat. Note that the Gulf of California surface water composition is similar to the composition of open-ocean seawater.

Sediment cores were collected at each site to a depth of ~50 cm using 7.5 cm thin-walled butyrate core liners. Following lithologic description, each core was sectioned into 1 cm sample intervals and a portion dried at low heat (40°C) and lightly ground in an alumina ceramic mortar and pestle for further analysis. A sample of mud-rich subtidal surface sediment from near the Inlet to the tidal flat, exposed to normal salinity surface water, was also obtained for comparison with the hypersaline tidal flat sediments. It is assumed that this Inlet sample is representative of the precursor mud-rich siliciclastic sediment initially deposited on the supratidal mud flats. This assumption is reasonable because most of the supratidal mud flat sediment was redeposited from offshore inter- and sub-tidal zones during periodic tidal flooding events (Thompson, 1968).

XRD analyses were obtained on selected bulk samples from each of the three cores and the Inlet sample to verify the major lithologies in the mud flat and to select representative samples for clay-separate XRD and STEM/AEM analyses. Portions of the dried, homogenized bulk samples were repeatedly sieved and ground to <38 μm and mounted on glass slides as acetone smears for XRD analyses. Semiquantitative estimates of mineral proportions were obtained by comparing intensity ratios of mineral peaks relative to

https://doi.org/10.1346/CCMN.1999.0470302 Published online by Cambridge University Press

quartz peaks with established mineral-quartz intensity ratios in standard mixtures, recognizing that such estimates have inherently large errors to 20 wt. % (*e.g.*, Moore and Reynolds, 1997).

The <2-μm clay separate fraction was obtained for samples from clay-rich zones near the top and bottom of the core, from each site on the mud flat, and from the marine Inlet sample. Undried and unground material was suspended in distilled water in 50 ml centrifuge tubes. Because of severe flocculation, sodium metaphosphate was added to the mud flat samples to disperse the clays. The <2 μm fraction was obtained by centrifugation (Jackson, 1969) from a single supernatant fraction, filtered (<0.45 μm), and transferred to a glass slide using the method of Drever (1973). The XRD analyses were carried out using a Philips model XRG 3100 diffractometer operated at 35 kV and 15 mA, using CuKα radiation, a scintillation detector with pulse height analyzer, theta-compensating slits, 0.5 mm (0.5°) receiving slit, and graphite-crystal monochromator. Digitally recorded patterns (step size of 0.01 °2θ and count rate of 1 s/step) were analyzed with a computer program written at the University of Michigan.

A second set of XRD experiments was done on Mg^{2+}- and K^{+}-saturated samples at Rutgers University. Samples from the Inlet and the Site 3 43–44 cm interval were placed in solutions of 1 N KCl and 1 N $MgCl_2$. The samples were mixed in an ultrasonic bath for 20 min, then repeatedly rinsed with distilled water and centrifuged at high speed (~3500 rpm) until no AgCl precipitated from the supernatant water with the addition of $AgNO_3$ (*e.g.*, Jackson, 1969). The <2-μm clay fraction was obtained by centrifugation and filtration and transferred to glass slides as described above. XRD patterns were obtained on air-dried, ethylene glycol solvated, and heated (300°C and 550°C) specimens. The XRD analyses were carried out using a General Electric XRD-5 diffractometer operated at 40 kV and 20 mA, using Ni-filtered CuKα radiation, a scintillation detector, 1° entrance slit and 0.2° receiving slit. Strip-chart patterns were obtained at a rate of 2° m^{-1} and peak positions determined manually.

TEM analyses of microtextures, structures and compositions of clay minerals in the hypersaline sabkha and marine Inlet samples were carried out using a Philips CM-12 STEM operated at 120 kV with a beam current of ~20 μA. Samples were prepared by two methods (*e.g.*, Peacor, 1992): (1) Moist sediment was placed in isopropyl alcohol and suspended clay particles were picked up on a 3 mm lacy C-coated Cu-grid. The clay particles obtained are thus aligned with (00*l*) planes approximately perpendicular to the electron beam (*c** parallel to beam). (2) Globules of moist mud were placed on a flat surface of hardened castolite acrylic resin and a second layer of resin placed on top and allowed to harden. Thin sections were prepared by cutting the "sandwiched" globules approximately perpendicular to bedding and mounting them on a glass slide using "sticky wax". No water was used in the cutting or grinding procedures. A 3 mm aluminum washer was attached to the area of interest with epoxy, the washer and sample were removed from the glass slide by melting the wax, and the sample was ion-thinned. These procedures were designed to preserve original textures and to permit observation of (00*l*) lattice planes parallel to the electron beam (*c** perpendicular to the beam).

Lattice fringe images were obtained at 75,000–100,000× magnification, using mainly over-focus (~100 nm) conditions to maximize contrast related to compositional differences between adjacent lattice fringes (*e.g.*, Veblen *et al.*, 1990). A camera length of 770 mm and selected area aperture of 10 μm was used to obtain SAED patterns. Great care was taken to obtain SAED patterns in regions composed of a packet of layers attributed to a single crystallite, or on grains isolated in the impregnating material.

Impregnation in castolite resin stabilizes the sample without permanently expanding smectite-like layers as with LR White Resin (*e.g.*, Kim *et al.*, 1995), a technique now routinely employed but not available at the time of this study. Under the high-vacuum conditions of the STEM, smectite-like layers commonly collapse to ~10 Å (Ahn and Peacor, 1989), and it is not always possible to distinguish collapsed smectite layers in lattice fringe images from mixed-layer illite-smectite (I-S), illite, or muscovite layers except under over-focus conditions of ~100 nm. Even so, in the present study, smectite could be distinguished from I-S, illite, and/or muscovite in these acrylic-impregnated samples. The smectite packets generally have wavy and irregular lattice fringes with spacings between 11–13 Å. The SAED patterns of such material are consistent with partial turbostratic stacking (presence of both (*hk*0) and (*h*0*l*) reflections in a single pattern) and $1M_d$ polytypism (presence of diffuseness and smearing of $k \neq 3n$ reflections parallel to *c**) (*e.g.*, Peacor, 1992; Dong and Peacor, 1996). Illite and/or muscovite packets are generally coarser-grained, have very straight and uniform 10-Å lattice fringe spacings, and SAED patterns indicating more ordered stacking sequences and some 2*M* polytypism.

Chemical (AEM) analyses were obtained using a Kevex Quantum System with the Philips CM-12 STEM operated in scanning mode using a 50-Å diameter spot rastered over 50 nm^2 with analytical resolution of ~10–20 individual 10-Å clay layers (Peacor, 1992). Data were reduced assuming thin-film conditions (Lorimer and Cliff, 1976). Jiang *et al.* (1990a) and Jiang *et al.* (1990b) describe other experimental conditions, standards, and analyses of spectra. AEM analyses obtained from both grain mounts and impregnated ion thinned samples (Tables 2 and 3) were

Table 2. Smectite $d(001)$-values determined by X-ray diffraction methods.

Sample	Inlet		Site 3 43–44 cm	
Preparation	Air-dried	Ethylene glycol solvated	Air-dried	Ethylene glycol solvated
Unsaturated	14.1	17.0	14.4	17.1
K^+-Saturated	12.4	17.1	15.5	17.2
Mg^{2+}-Saturated	15.8	17.1	16.3	17.0
Heated 300°C[1]	10.1	n.d.	10.1	n.d.
Heated 550°C[1]	10.1	n.d.	10.1	n.d.

[1] Both K^+- and Mg^{2+}-saturated samples. n.d. = not determined.

normalized to 44 negative charges (22 oxygens). This normalization procedure includes the alkali content in the calculation of cation proportions. Some diffusional loss of K due to beam-sample interaction can occur during AEM analyses (van der Pluijm *et al.*, 1988), especially when packet sizes are small, as in this study. However, care was taken to minimize such loss by incorporating the entire grain in the area of the rastered beam (*e.g.*, Banfield *et al.*, 1991a, 1991b). The Na content was not included in the normalization calculation for smectite mounted on lacy-C Cu-grids due to interference from Cu L-lines in the spectra, or for smectite from the hypersaline mud flat samples due to halite contamination. The omission of Na from the mineral formula does not seriously affect the results because Na was determined to be a minor constituent (<0.1 cation/22 oxygen atoms; Table 3) in smectite from the marine Inlet sample, the assumed precursor material.

RESULTS

Clay mineralogy

The mineral proportions in the bulk Inlet sample are estimated to be ~45% total clay, ~35% quartz, ~5% potassium feldspar, ~5% plagioclase feldspar, ~5% calcite, and ~5% dolomite (±20% by weight) as determined by XRD methods (Figure 2A). The siliciclastic assemblage in the Salina Ometepec sabkha samples is essentially the same as the Inlet sample, but differs substantially in the content of evaporite minerals gypsum and halite. Two examples spanning the range in evaporite mineral content are compared in Figure 2B and 2C. The shallow 2–4 cm interval at the most landward Site 1 contains a small proportion of evaporite minerals (<25 wt. %; Figure 2B), whereas the diffraction pattern for the 43–44 cm sample from the most seaward Site 3 is more typical of the mud flat lithologies and contains a relatively high proportion of gypsum and halite (>50 wt. %; Figure 2C). Dolomite and celestite are also present and calcite is absent in the latter sample. The diffraction peak at ~19.8 °2θ results from the combined (*hk(l)*) reflections from smectite, illite-mica, and kaolinite peaks in randomly oriented sample mounts. A broad tail toward the high 2θ-side of the peak was interpreted to indicate the presence of turbostratic stacking in smectite (*e.g.*, Moore and Reynolds, 1997). Some tailing of this peak is observed in the diffraction patterns in Figure 2 and may imply that smectite is turbostratically stacked. However, because of the interference of the quartz peak at ~20.80 °2θ and the superposition of several clay diffraction patterns at ~19.8 °2θ, we cannot unequivocally assign this observed tailing to turbostratic stacking in smectite alone.

Table 3. Structural formulae of smectite in Inlet samples, Gulf of California, calculated from AEM analyses.

Sample	GM SME2	GM SME5	IM SME7	IM SME11
Si	7.15	7.26	7.33	7.29
Al^{iv}	0.85	0.74	0.67	0.71
Charge	−0.85	−0.74	−0.67	−0.71
Al^{vi}	2.93	2.88	2.72	2.80
Fe(III)[1]	0.56	0.59	0.67	0.60
Mg	0.61	0.66	0.78	0.60
Mn	0.05	0.03	0.00	0.00
Ti	0.00	0.00	0.00	0.00
Cr	0.06	0.00	0.00	0.00
Charge	−0.65	−0.69	−0.78	−0.60
Na	n.d.	n.d.	0.00	0.00
K	0.88	0.67	0.59	0.80
Ca	0.00	0.08	0.16	0.00
Charge	0.88	0.84	0.92	0.80
Mg/(Mg + Fe(III))	0.52	0.53	0.54	0.50
Mg/(Al^{vi} + Mg + Fe(III))	0.15	0.16	0.19	0.15

Normalized to 22 oxygens (44 negative charges).
[1] All Fe calculated as Fe(III).
n.d. = Not determined due to Cu interference from Grid. GM = Grain mount sample. IM = Ion milled sample.

The presence of expandable smectite in the <2-μm clay separate from the Inlet sample is indicated by the shift in the (001) peak from ~14.1 Å (~6.3 °2θ) in the air dried pattern to ~17 Å (~5.2 °2θ) in the ethylene glycol solvated sample (Figure 3A; Table 2). The presence of higher-order diffraction peaks at ~8.5 Å, and 5.6 Å, in the glycol solvated sample (Figure 3A), and absence of reflections between ~10–17 Å or at >17 Å, indicate that smectite does not contain mixed-layers of illite (Reynolds, 1980; Moore and Reynolds, 1997). The $d(001)$-values of this peak in air-dried, ethylene glycol solvated, and heated K^+- and Mg^{2+}-saturated samples (Table 2) do not indicate that a non-smectite phase such as vermiculite or other mixed-layer clay is present (*e.g.*, Jackson, 1969; Moore and Reynolds, 1997). Non-expandable 10-Å illite and/or mica and 7-Å kaolinite are also present in the sample. The presence of trace chlorite was confirmed in a sample heated to 550°C (pattern not shown) by the presence of small peaks at $d(001)$ ~14.2 Å and $d(003)$ ~3.54 Å.

https://doi.org/10.1346/CCMN.1999.0470302 Published online by Cambridge University Press

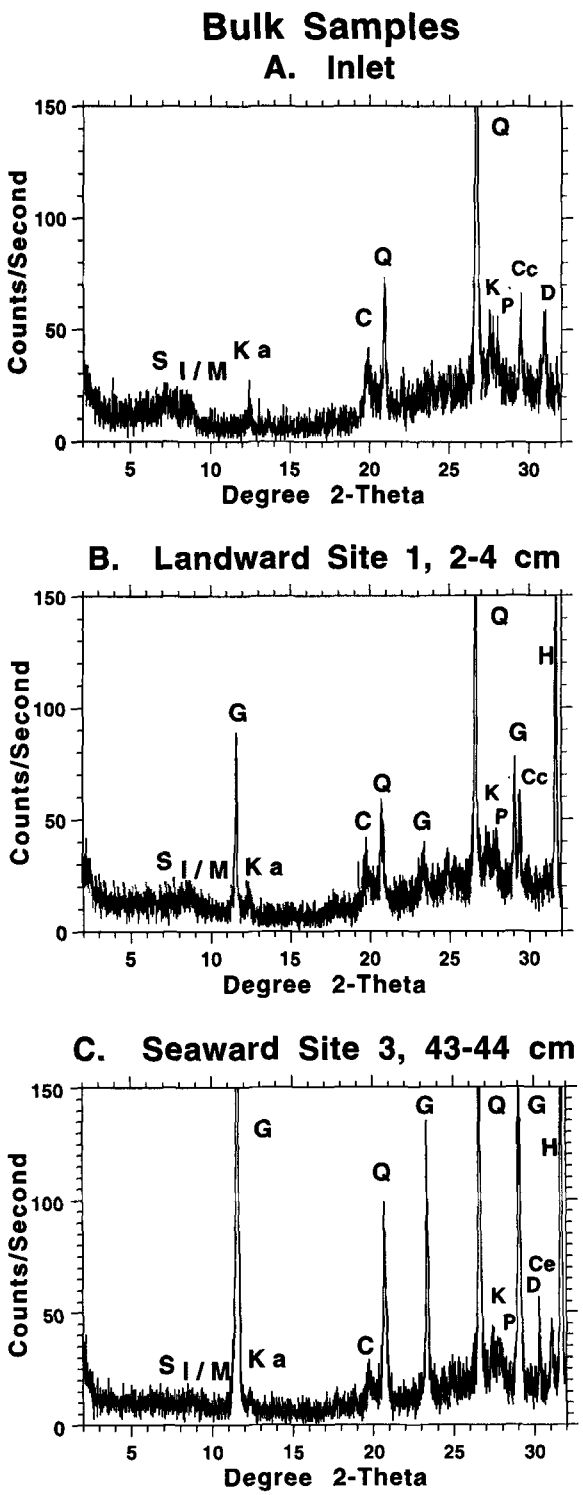

Figure 2. Bulk sample XRD patterns: A) Gulf of California Inlet sample (no evaporites, marine environment), B) most landward salina sample (<50 wt. % evaporites), (Site 1, 2–4 cm) and (C) most seaward mud flat sample, (>50 wt. % evaporites), (Site 3, 43–44 cm). Abbreviations: C = (*hk(l)*) reflection from clay minerals, Cc = calcite, Ce = celestite, D = dolomite, G = gypsum, H = halite, I/M = 10-Å illite or mica material, K = K-feldspar, P = plagioclase feldspar, Q = quartz, S = smectite.

The XRD patterns of the oriented air-dried and ethylene glycol-solvated <2-μm fractions of the two mud-flat samples are shown in Figure 3B and 3C, respectively. The character of the expandable smectite (001) diffraction peaks in the hypersaline mud flat samples differs from that observed in the Inlet sample. The smectite (001) peak in the air-dried sample occurs at a slightly larger *d*-value of 14.4 Å than in the Inlet sample, and similarly, the *d*(001)-values for the K^+- and Mg^{2+}-saturated samples are correspondingly larger (Table 2). The smectite (001) peaks shift to ~17 Å in all the ethylene-glycol solvated samples as in the Inlet sample. There is also a broad shoulder extending to the low 2θ side of the peak in the pattern from the shallow landward Site 1 sample and a hint of a superlattice peak at ~23.5 Å in the pattern of the seaward Site 3 sample (see arrows, Figure 3B and 3C). These observations suggest possible interlayering of an ~10-Å with an ~14-Å phase. A similar superlattice peak was observed in the diffraction patterns of trioctahedral Mg-rich stevensite by Brindley (1955) who suggested it may represent interlayering of talc-like and smectite-like layers. A trace of chlorite was also identified in the samples heated to 550°C by the presence of small diffraction peak at *d*(001) ~14.2 Å and *d*(003) ~3.54 Å. Little difference in the relative proportions of illiter-mica or kaolinite was observed between the Inlet and mud flat samples. The presence of a broad shoulder and possible superlattice peak at ~24 Å, and the larger *d*(001)-values of air-dried clay separates, are consistent with the presence of an expandable smectite or mixed-layer phase of different composition or structure in the hypersaline sabkha sediments relative to the normal salinity Inlet sample.

Texture and structure of smectite

The XRD results suggest that the principal differences in clay mineral assemblages in the hypersaline mud flat samples may be related to the formation of a trioctahedral smectite; STEM analyses focused on characterization of this phase. The TEM images from the marine Inlet sample mounted on a lacy-C Cu-grid such that *c** is parallel to the electron beam (Figure 4) show that smectite occurs as thin flat sheets with generally irregular outlines, although some grains have subhedral outlines displaying 60 or 120° angles consistent with pseudohexagonal symmetry. The SAED patterns taken at the thin edge of such grains show diffuse rings of spots with some sharp single-crystal hexanet reflections, or two or more such patterns related by rotation about *c** imbedded in the diffuse rings (inset, Figure 4). The inner ring of spots corre-

https://doi.org/10.1346/CCMN.1999.0470302 Published online by Cambridge University Press

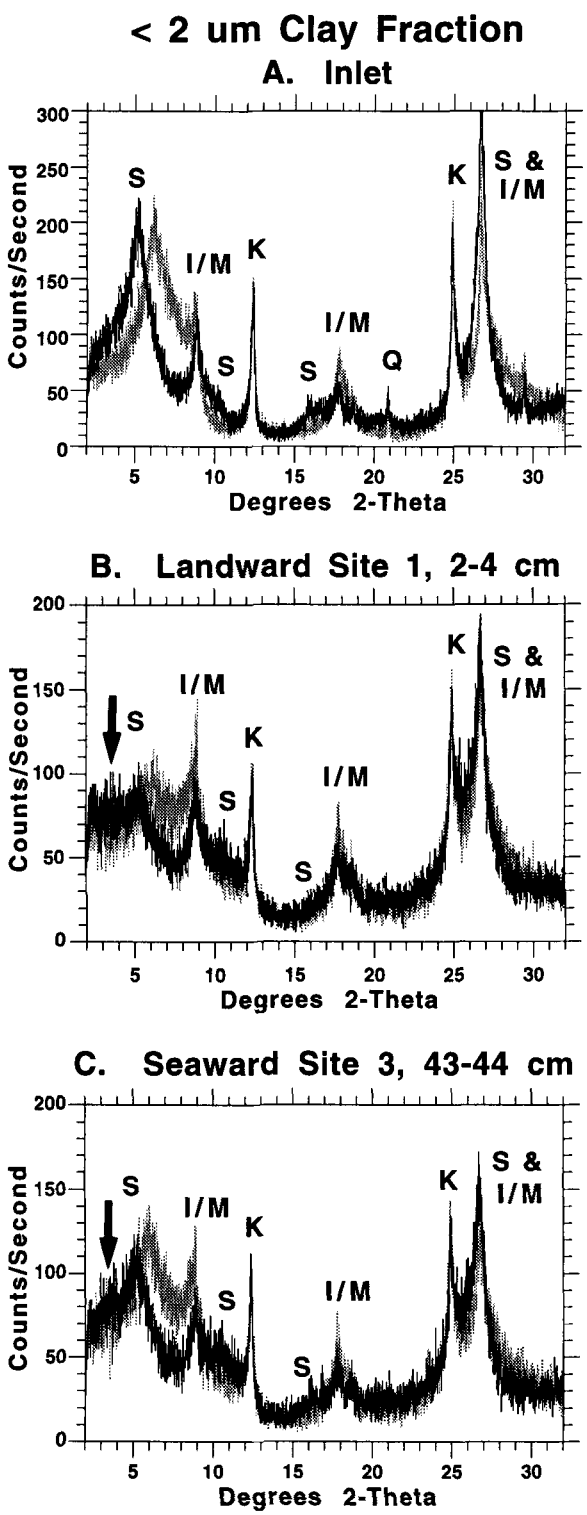

Figure 3. XRD patterns of oriented <2 μm air-dried (stippled line) and ethylene glycol solvated (solid line) clay fractions: A) Gulf of California marine Inlet sample, B) most landward, salina sample (Site 1, 2–4 cm), and C) most seaward, sabkha sample (Site 3, 43–44 cm). Abbreviations: I/M = 10-Å illite or mica material, K = kaolinite, Q = quartz, S = smectite. Arrows indicate the possible superlattice diffraction peak at ~24 Å.

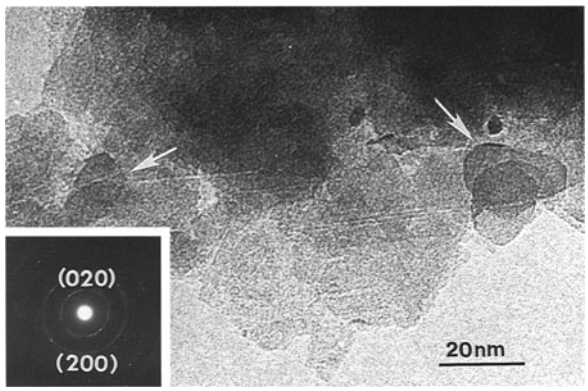

Figure 4. STEM image of smectite aggregate mounted on a lacy-C, Cu-grid oriented with c^* parallel to the electron beam. Arrows indicate subhedral pseudohexagonal 60 and 120° grain boundaries SAED pattern (inset) shows diffuse rings with only a few discrete spots, imbedded in the rings, related by pseudohexagonal symmetry, indicating that layer stacking is predominantly turbostratic.

sponds to (020) reflections and their symmetrical equivalents (~4.6 Å) and the second circle to (200) reflections and their symmetrical equivalents (~2.7 Å). The presence of sharp hexanet reflections implies some local coherence between individual layers. The diffuse nature of the diffraction rings is consistent with overall disordered turbostratic stacking of individual smectite layers or simply overlapping of many individual smectite packets in the aggregate grain. Several individual crystallites, which range from ~20–100 nm in diameter, commonly cluster to form such aggregates. These smectite grains are readily distinguished from illite and/or muscovite and kaolinite crystals, which are much larger (>~0.1 μm) and have sharp hexanet SAED patterns (not shown). Identification of smectite *vs* illite and kaolinite was confirmed by AEM analyses.

The TEM images of smectite in an acrylic resin-impregnated Inlet sample, oriented with c^* perpendicular to the electron beam, show typical microtextures (Figure 5). Individual smectite crystallites consist of small packets (from three to ten layers) with wavy, irregular lattice fringes. Several crystallites, with subparallel orientations with respect to one another, cluster to form larger aggregates (Figure 5A). Only small portions of these aggregates are in the proper orientation to yield clear lattice fringe images (Figure 5B). Spacing between lattice fringes is variable, ranging from ~11–13 Å. The larger spacings are consistent with the thickness observed for smectite layers impregnated in LR white resin (*e.g.*, Dong and Peacor,

https://doi.org/10.1346/CCMN.1999.0470302 Published online by Cambridge University Press

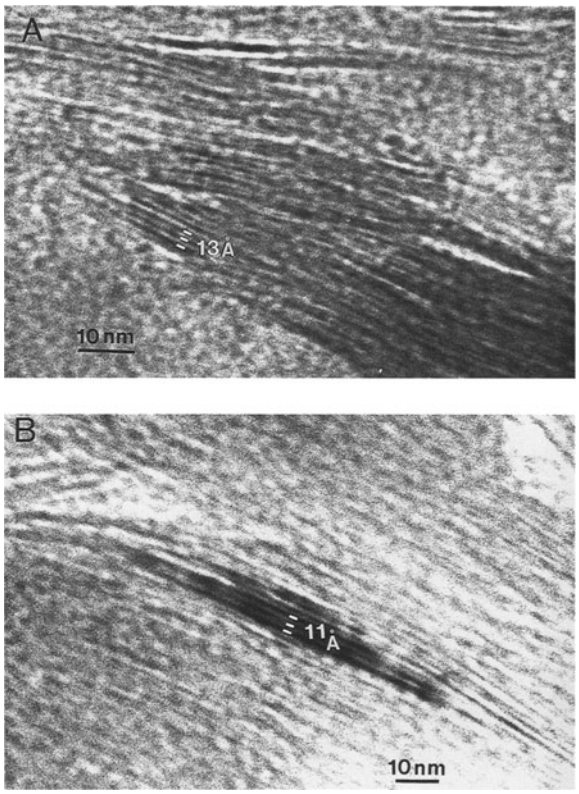

Figure 5. STEM images of the ion-thinned normal-marine Inlet sample with c^* of smectite crystallites oriented approximately perpendicular to the electron beam. A) Smectite occurs in subparallel aggregates, composed of individual crystallites containing from three to ten layers. Lattice fringes are wavy and irregular with interplanar spacings of ~13 Å, indicating partial expansion by the castolite resin. B) A smectite crystallite composed of about five individual layers with interplanar spacing of ~11 Å indicating partial collapse of lattice planes. Crystallite length is ~100 nm, typical of smectite from the marine Inlet sediment.

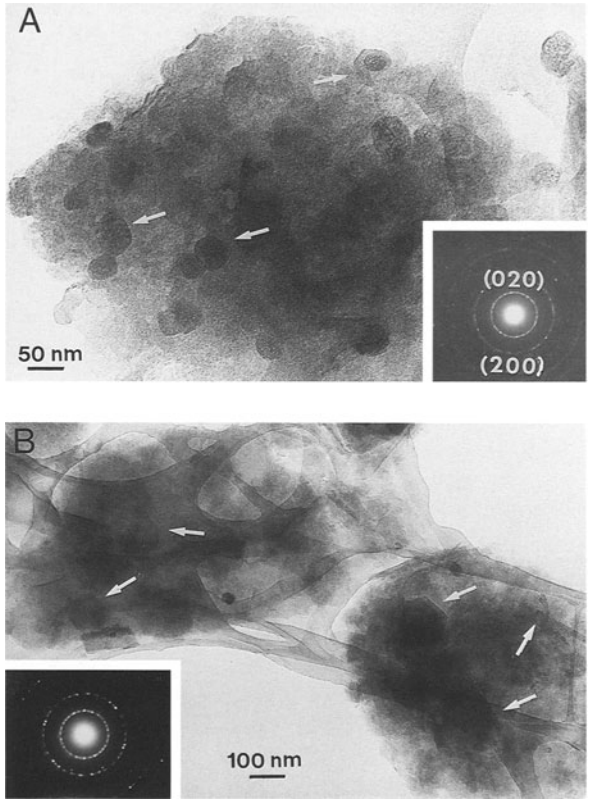

Figure 6. STEM images of smectite aggregate from the most seaward sabkha mud flat (Site 3) mounted on a lacy-C Cu-grid oriented with c^* parallel to the electron beam. A) Smectite from the shallowest interval (0–1 cm) with crystallites <50 nm in diameter; arrows indicate pseudohexagonal 60 and 120° grain boundaries. The SAED pattern (inset) shows diffuse rings with superimposed sets of discrete spots related by pseudohexagonal symmetry and related by random rotation about c^*, consistent with larger domains of coherent layers than were present in the marine Inlet sample (Figure 4). B) Smectite from a deeper interval from Site 3 (43–44 cm) contains larger (~100–250 nm) pseudohexagonal euhedral crystallites and some lath-shaped crystallites (arrows). The SAED pattern (inset) shows more discrete spots than in the shallower sample in (A), indicating a higher degree of order. The innermost ring of diffraction spots corresponds to (020) and symmetrically equivalent reflections (~4.6 Å); the second ring corresponds to (200) and symmetrically equivalent reflections (~2.7 Å).

1996), whereas the smaller spacings are due to imperfect stabilization of the sample in the acrylic resin and partial collapse of some smectite layers to ~10 Å in the high vacuum TEM environment (*e.g.,* Ahn and Peacor, 1989). It was nearly impossible to obtain SAED patterns of smectite from the Inlet sample in this orientation because of the small size and poor crystallinity of the smectite. Faint patterns disappear within a few seconds exposure time.

The TEM images of clay separates from hypersaline mud flat samples mounted on lacy-C Cu-grids show textural evidence for the formation of an authigenic clay phase. For example, in the shallowest 0–1 cm interval at the most distal Site 3, TEM images of clay aggregates contain many small (~20–40 nm), subhedral, pseudohexagonal-shaped crystallites (Figure 6A). In the deeper 43–44 cm interval, larger (100–250 nm), more euhedral pseudohexagonal and lath-shaped crystallites are present (Figure 6B). The SAED patterns of such aggregates (inset, Figure 6A and 6B) still contain diffuse rings of spots consistent with turbostratic stacking of layers or overlap of many small crystallites related by random rotation about c^*. However, there is also a greater proportion of discrete reflection spots with hexanet symmetry imbedded within the diffuse rings, especially for the sample from the deeper interval (Figure 6B). The better-resolved, discrete reflections indicate larger and more coherent smectite domains in hypersaline mud flat sediments as compared with the marine Inlet sediments described earlier.

https://doi.org/10.1346/CCMN.1999.0470302 Published online by Cambridge University Press

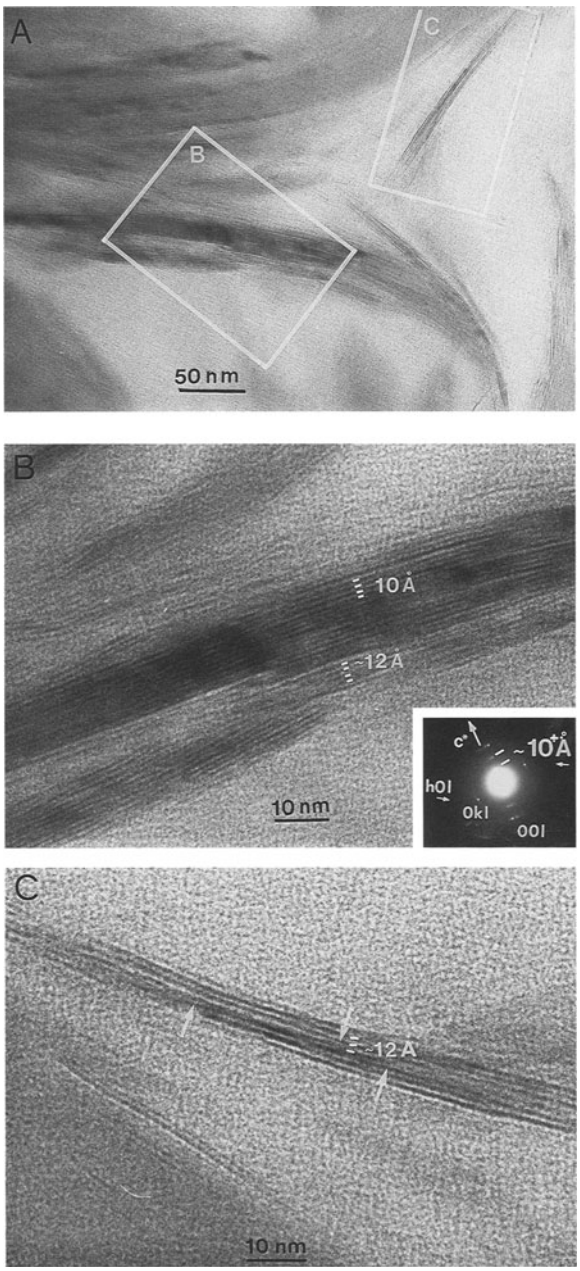

Figure 7. STEM image of ion-thinned sabkha mud flat sample (seaward Site 3, 43–44 cm) mounted with c^* of smectite oriented approximately perpendicular to the electron beam. A) The low magnification image shows a large detrital illite grain (i) and smaller wispy smectite crystallites (s). B) Enlargement of (A) shows that the detrital illite grain has relatively straight and uniform lattice fringes with regular interplanar spacing of 10 Å. In contrast, lattice fringes of smectite crystallites are more irregular with interplanar spacing ~12 Å. The SAED pattern of smectite (inset) shows diffuse (00*l*) reflections slightly larger than 10 Å consistent with partially collapsed smectite layers. Diffuseness parallel to c^* indicates some larger interplanar spacings, while the fanning of reflections perpendicular to c^* result from the subparallel nature of adjacent smectite crystallites. C) Enlargement of an isolated wispy smectite crystallite shown in (A) with irregular lattice fringes with several dislocations (arrows) and interplanar spacing of ~12 Å. Smectite crystallites are still only a few layers thick (<10), but longer than crystallites in the marine Inlet sample in Figure 5.

A low magnification TEM image of an ion-milled acrylic-impregnated hypersaline mud flat sample (Figure 7A) shows a typical aggregate of clay crystals. The large crystal (~3 μm) in the image is interpreted as illite because of the relatively straight and uniform 10-Å lattice fringe spacings, the relatively large packet size (~20 layers) (Figure 7B), and compositions that are K- and Al-rich as determined by AEM analyses. Associated with the illite grain are smaller (<0.2 μm) wispy crystallites interpreted to be smectite because of their irregular ~12-Å lattice fringe spacings and smaller packet size (<7 layers) (Figure 7B and 7C).

The SAED patterns of smectite (Figure 7B) show ~10-Å and larger (00*l*) electron diffraction reflections consistent with partially collapsed smectite layers. The reflections are diffuse parallel to c^*, consistent with the presence of some >10-Å layers. The fanning of reflections perpendicular to c^* is consistent with the subparallel nature of adjacent smectite grains (Figure 7B). The SAED patterns also show faint (0*kl*) reflections. Polytype information is provided only by such (0*kl*) reflections (*e.g.*, (021) or (041) or pseudohexagonal equivalents (*e.g.*, (111) or (221) for which $k \neq 3n$ (Bailey, 1988; Peacor, 1992; Dong and Peacor, 1996). The (0*kl*) reflections in SAED patterns (inset, Figure 7B) are poorly defined, nonperiodic, and diffuse parallel to c^*, consistent with disordered stacking of polytypes referred to as $1M_d$ polytypism (*e.g.*, Peacor, 1992; Dong and Peacor, 1996). Disordered, turbostratic stacking is indicated by the presence of both (0*kl*) and faint (*h*0*l*) reflections (or the pseudohexagonal equivalents) in the same SAED pattern.

Smectite chemical analyses

Representative structural formulae calculated from AEM chemical analyses of smectite in the marine Inlet sample are given in Table 3. Analyses were obtained from near crystallite edges in the lacy-C Cu-grid grain mounts or from individual crystallite packets in ion-milled acrylic-impregnated samples. These regions were confirmed to be smectite, as determined by the presence of wavy, irregular lattice fringes in TEM images of ion-milled samples, diffuse (0*kl*) spots in SAED patterns of ion milled samples, or diffuse rings in SAED patterns of grain-mounted samples, indicating disordered turbostratic structures. Compositions are Si-rich and K- and Al-deficient relative to ideal muscovite. Si contents range from 6.9 to 7.3 cations/22 oxygen atoms with 7.1 to 7.2 cations/22 oxygen atoms typical.

https://doi.org/10.1346/CCMN.1999.0470302 Published online by Cambridge University Press

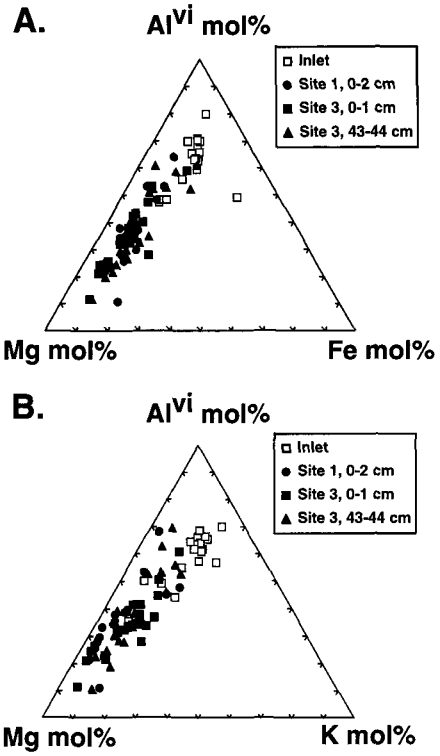

Figure 8. A) Molecular proportions of octahedral Al:Mg:Fe as determined by AEM analyses of individual smectite crystallites. B) Molecular proportion of octahedral Al and Mg, and interlayer K as determined by AEM analyses of individual smectite crystallites. The compositional evolutionary trend in the data from Al-rich to Mg-rich is explained most simply by formation of Mg-rich smectite, with a K-content virtually identical to that of the precursor Inlet smectite.

The molar octahedral Al:Mg:Fe proportions (Figure 8A) indicate that the Inlet smectite is dominated by an Al-rich dioctahedral component with a composition close to a beidellite end-member (*e.g.*, $R^{+}_{0.67}Al_4(Si_{7.34}Al_{0.67})O_{20}(OH)_4$ (Moore and Reynolds, 1997). Principle non-beidellite components are the substitution of dioctahedral Fe^{3+} for ^{vi}Al (nontronite end-member) and substitution of a saponite end-member (*e.g.*, $R^{+}_{0.67}(Al_{0.67}Mg_{5.34})(Al_{1.34}Si_{6.68})O_{20}(OH)_4$). Mg/(Mg + Fe) mole ratios are ~0.50 and Mg/(^{vi}Al + Mg + Fe) ratios are <0.20 (Table 3). The trend toward more Mg-rich compositions may indicate the presence of some Mg-rich smectite derived from the hypersaline mud flat described in more detail below. Total octahedral occupancy ranges from 4.1 to 4.4 cations/22 oxygen atoms.

The AEM analyses indicate that K^+ is the dominant interlayer cation, often being the only detectable cation (Table 3). The K^+ contents range from 0.3 to 0.9 cations/22 oxygen atoms. In ion-milled samples, Na^+ and Ca^{2+} contents range from 0 to 0.3 cations/22 oxygen atoms, but are always less than K^+ contents in a given analysis (Table 3). Na^+ could not be determined for smectite in grain mounted samples due to the interference of Cu from the Cu-grids. The total alkali contents of 0.8 to 1.4 cations/22 oxygen atoms are generally insufficient to balance the net negative tetrahedral plus octahedral charges (assuming pure dioctahedral compositions) due, in part, to the diffusional loss of alkalis (especially K^+) during AEM analyses (*e.g.*, van der Pluijm *et al.*, 1988). Substitution of Mg^{2+} in vacant octahedral sites results in a lower net negative charge on the octahedral sheets (*e.g.*, Moore and Reynolds, 1997), relative to an ideal dioctahedral end-member. The relatively small interlayer cation concentrations (<~1.0 cation/22 oxygen atoms) and net negative tetrahedral and octahedral sheet charges are consistent with low-charge smectite (*e.g.*, Moore and Reynolds, 1997). The aluminous dioctahedral compositions of smectite from the Inlet can be approximated by the formula $K_{0.7}(Al_{3.3}Fe^{3+}Mg_{0.5})(Al_{0.7}Si_{7.3})O_{20}(OH)_4$.

The structural formulae determined from AEM analyses of individual smectite crystallites in grain mounts and ion-milled samples from the hypersaline mud flat samples are given in Table 4. Again, compositions are Si-rich and K- and Al-deficient, consistent with smectite compositions. The Si contents range from 6.8 to 7.5 cations/22 oxygen atoms with net negative charges on the tetrahedral sheets of 0.5 to 1.2 cations/22 oxygen atoms. Mole ratios of octahedral Al:Mg:Fe (Figure 8A) of smectite from the hypersaline mud flat are significantly more Mg-rich relative to the marine Inlet sample. The data trend from Al-rich compositions close to that of the Inlet sample, the presumed precursor material, toward the Mg-rich corner of the diagrams. Total octahedral site occupancies range from 4.6 to 5.8 cations/22 oxygen atoms indicating that a significant trioctahedral component is present. Smectite Mg/(Mg + Fe) and Mg/(^{vi}Al + Mg + Fe) mole ratios are larger than in the Inlet sample and range from 0.7 to 0.9 and 0.3 to 0.8, respectively (Table 4). Smectite compositions suggest the presence of up to 75% saponitic end-member component, with the remainder composed of beidellite and montmorillonite end-member components. Similar trends toward trioctahedral Mg^{2+}-rich compositions were observed by Banfield *et al.* (1991b) for authigenic smectite formed in the alkaline hypersaline playa Lake Abert.

Potassium is the dominant interlayer cation in the hypersaline mud flat smectite, and compositions range from 0.3 to 0.8 K-cations/22 oxygen atoms (Table 4). Ca^{2+}, if detected, is always present in lower concentrations than K^+ in a given analysis, and in general, in lower concentrations than observed in Inlet-sample smectite (<0.2 cations/22 oxygen atoms). The molecular proportions of Al:Mg:K (Figure 8B) in the smectite from the hypersaline mud flat indicate that the K^+ content does not differ significantly from the marine Inlet sample. The data suggest that a K^+-rich illite

Table 4. Structural formulae of smectite in hypersaline sabkha samples, Salina Ometepec, calculated from AEM analyses. Site 1, Landward; Site 3, Seaward.

Sample no.	Site 1 2–4 cm GM SME7	Site 1 2–4 cm GM SME12	Site 1 2–4 cm GM SME17	Site 3 0–1 cm GM SME12	Site 3 0–1 cm IM SME6	Site 3 0–1 cm IM SME9	Site 3 43–44 cm GM SME9	Site 3 43–44 cm IM SME13	Site 3 43–44 cm IM SME15
Si	7.45	7.01	6.81	7.32	6.94	7.04	7.32	6.84	7.01
Al^{iv}	0.55	0.99	1.19	0.68	1.06	0.96	0.68	1.16	0.99
Charge	−0.55	−0.99	−1.19	−0.68	−1.06	−0.96	−0.68	−1.16	−0.99
Al^{vi}	2.00	1.94	2.75	1.74	1.24	2.15	1.74	0.67	2.37
Fe(III)[1]	0.46	0.52	0.40	0.44	0.43	0.35	0.44	0.53	0.38
Mg	2.49	2.66	1.11	2.78	3.78	2.53	2.60	4.45	1.86
Mn	0.00	0.00	0.06	0.00	0.00	0.00	0.00	0.05	0.03
Ti	0.00	0.00	0.07	0.00	0.00	0.00	0.06	0.00	0.00
Cr	0.05	0.00	0.06	0.00	0.00	0.00	0.04	0.00	0.00
Na[2]	n.d.	n.d.	n.d.	n.d.	—	—	n.d.	—	—
K	0.31	0.28	0.78	0.51	0.51	0.40	0.59	0.59	0.83
Ca	0.05	0.00	0.07	0.00	0.00	0.00	0.00	0.00	0.00
Charge	0.41	0.28	0.93	0.51	0.51	0.04	0.59	0.59	0.83
Mg/(Mg + Fe(III))	0.84	0.84	0.74	0.86	0.90	0.88	0.86	0.89	0.83
$Mg/(Al^{vi} + Mg + Fe(III))$	0.50	0.52	0.26	0.56	0.69	0.50	0.54	0.79	0.40

Normalized to 22 oxygens (44 negative charges).

[1] All Fe calculated as Fe(III).

[2] Na excluded from normalization of ion milled analyses due to halite contamination. n.d. = Not determined due to Cu interference from grid.

GM = Grain mount sample. IM = Ion milled sample.

mineral phase is *not* forming as a result of near surface diagenesis in the hypersaline environment. Furthermore, Mg^{2+} does not appear to be a significant interlayer cation. Similar trends in smectite composition were observed by Banfield *et al.* (1991b) from hypersaline Lake Abert sediments. Thus, the AEM-determined compositions of individual smectite crystallites from the Salina Ometepec sabkha environment are consistent with K- and Mg-rich, low-charge smectite. The end-member composition is inferred to be $\sim K_{0.70}(Al_{0.70}Fe(III)_{0.5}Mg_{4.45})(Al_{1.2}Si_{6.8})O_{20}(OH)_4$.

Mg-SMECTITE AUTHIGENESIS: COMPATIBILITY WITH PORE WATER CHEMISTRY

The Salina Ometepec complex represents a relatively unique environment. Sediment mineralogy is dominated by a siliciclastic and evaporite mineral assemblage because the organic-poor nature of the sediments suppresses the formation of carbonate minerals. Importantly, dolomite, which commonly replaces calcite in other sabkha environments, as in Abu Dhabi (*e.g.*, Butler, 1969; Kinsman, 1969), remarkably, is absent. The lack of dolomite precipitation is expected to result in elevated Mg^{2+}/Ca^{2+} molar ratios and high Mg^{2+} concentrations in Salina Ometepec pore waters relative to the Abu Dhabi sabkha complex, where calcite precipitation and dolomite replacement occur. To evaluate the extent of Mg^{2+} enrichment in the Salina Ometepec pore waters and its possible role in Mg-smectite formation, the variation of Ca^{2+} concentrations and Mg^{2+}/Ca^{2+} ratios with SO_4^{2-} concentrations in Salina Ometepec surface and sediment pore waters (Martini, 1997) are plotted in Figure 9 and compared to Abu Dhabi waters (Butler, 1969). The data are superimposed on the established closed-system seawater evaporation trends of McCaffrey *et al.* (1987).

The Ca^{2+} *vs.* SO_4^{2-} concentrations of surface waters from the Gulf of California and the Salina Ometepec and dolomite-poor Abu Dhabi sabkhas superimpose on the established seawater evaporation trend (Figure 9A). The change in slope at SO_4^{2-} concentrations ~110 *mM* corresponds to the onset of gypsum precipitation. As evaporation increases beyond gypsum saturation, Ca^{2+} concentrations decrease with increasing SO_4^{2-} concentration. The Ca^{2+} (~30 *mM*) and SO_4^{2-} (~90 *mM*) concentrations of Salina Ometepec overlying waters (Figure 9A; Table 1) closely follow the expected trend for the evaporation of seawater not yet concentrated to the point of gypsum saturation.

The Ca^{2+} and SO_4^{2-} concentrations of surface waters from dolomite-rich Abu Dhabi sabkhas, however, show a marked increase in Ca^{2+} as a result of the equimolar exchange of Mg^{2+} for Ca^{2+} during dolomite replacement of previously precipitated calcite. The variable concentration of SO_4^{2-} in these waters is compatible with variable degrees of sulfate reduction typical of marine carbonates with differing amounts of organic-carbon and extents of bioturbation (*e.g.*, Walter and Burton, 1990; Walter *et al.*, 1993).

The expected variation in the Mg^{2+}/Ca^{2+} molar ratio with SO_4^{2-} concentration during seawater evaporation is shown in Figure 9B. The molar Mg^{2+}/Ca^{2+} ratio is ~5.0 to the onset of gypsum precipitation. At higher

https://doi.org/10.1346/CCMN.1999.0470302 Published online by Cambridge University Press

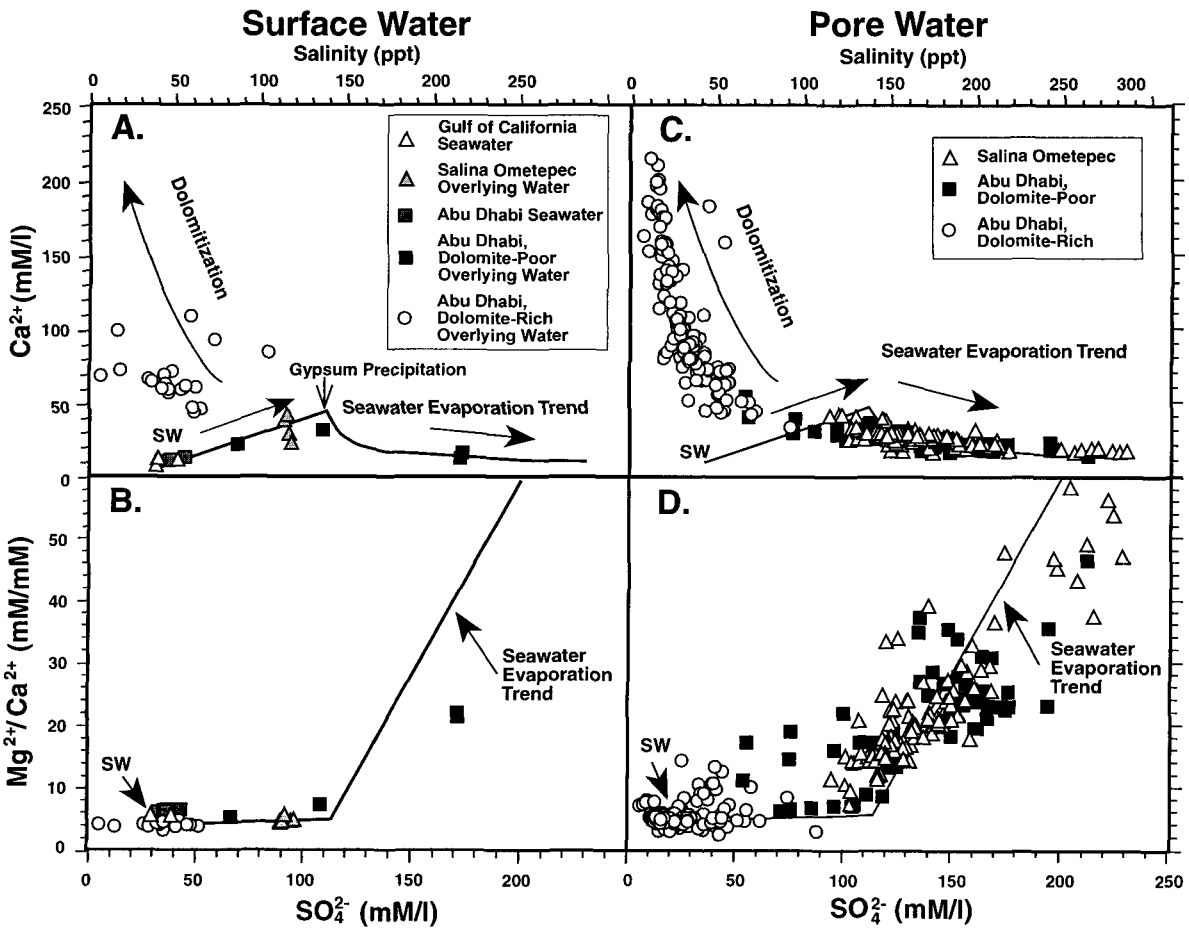

Figure 9. Concentration trends of Ca^{2+} *vs.* SO_4^{2-} and Mg^{2+}/Ca^{2+} *vs.* SO_4^{2-} of Gulf of California seawater, Salina Ometepec overlying (surface) and pore water (Martini, 1997) and Abu Dhabi sabkha overlying and pore water (Butler, 1969). The solid lines in each diagram represent the variation in Ca^{2+} with SO_4^{2-} or Mg^{2+}/Ca^{2+} with SO_4^{2-}, respectively, during evaporation of seawater (*e.g.*, McCaffrey *et al.*, 1987). The change in slope at ~110 mmol/l SO_4^{2-} corresponds to the onset of gypsum precipitation and removal of Ca^{2+} from the evaporating seawater. The Ca^{2+} concentration (A) and molar Mg^{2+}/Ca^{2+} ratio (B) in overlying water from the Gulf of California at the Inlet and Abu Dhabi lagoon plot at the expected seawater (SW) composition. The hypersaline Salina Ometepec pore water compositions conform to the expected trend for the normal evaporation of seawater into gypsum facies and have low Ca^{2+} concentrations (C) and high Mg^{2+}/Ca^{2+} molar ratios (D).

degrees of evaporation, the Mg^{2+}/Ca^{2+} ratio increases with increasing SO_4^{2-} concentration as a result of removal of Ca^{2+} from seawater during gypsum precipitation (*e.g.*, McCaffrey *et al.*, 1987). The Mg^{2+}/Ca^{2+} molar ratio Gulf of California and Abu Dhabi surface water is ~5.1, similar to normal seawater (Figure 9B; Table 1). As SO_4^{2-} concentration increases in water overlying the Salina Ometepec and the dolomite-poor Abu Dhabi sabkha, the Mg^{2+}/Ca^{2+} ratio remains ~5 until the onset of gypsum precipitation, and increases rapidly afterwards (Figure 9B). The Mg^{2+}/Ca^{2+} molar ratios in overlying water from the dolomite-rich portion of the Abu Dhabi sabkha are <5, consistent with removal of Mg^{2+} during dolomite precipitation.

The Salina Ometepec and Abu Dhabi dolomite-poor sediment pore water Ca^{2+} concentrations decrease with increasing SO_4^{2-} concentrations along the predicted seawater evaporation trend consistent with rapid removal of Ca^{2+} during gypsum precipitation and low degrees of SO_4^{2-} reduction (Figure 9C). Pore waters from dolomite-rich Abu Dhabi sediments show a marked increase in Ca^{2+} as a result of the equimolar exchange of Mg^{2+} for Ca^{2+} during dolomite replacement of previously precipitated calcite. The Mg^{2+}/Ca^{2+} molar ratio of Salina Ometepec and Abu Dhabi dolomite-poor pore waters increases to 60 with increasing evaporation and follows the predicted seawater evaporation trend consistent with gypsum precipitation (Figure 9D). In contrast, the Mg^{2+}/Ca^{2+} ratios of pore waters from dolomite-rich Abu Dhabi sediments are much lower (2–10) as a result of dolomite replacement of calcite.

https://doi.org/10.1346/CCMN.1999.0470302 Published online by Cambridge University Press

The elevated Mg^{2+}/Ca^{2+} ratio of Salina Ometepec sediment pore waters at high degrees of seawater evaporation indicates that Mg^{2+} concentrations are dominantly controlled by the evaporation into gypsum facies, and are not controlled by other precipitating phases such as dolomite. Thus, the elevated Mg^{2+} content potentially is available to form Mg-rich authigenic clay.

TEXTURAL AND CHEMICAL EVIDENCE FOR AUTHIGENIC SMECTITE FORMATION

Textural evidence

The primary textural evidence for the formation of authigenic smectite in the hypersaline mud flat sediments is the ubiquitous presence of tiny sub- to euhedral pseudohexagonal and lath-shaped crystallites to 250 nm in diameter as observed in TEM images (Figure 6). These tiny euhedral crystallites are absent in the Inlet sample; only smectite sheets with irregular crystallite outlines occur. Lath-shaped crystallites in particular are typical of first-formed authigenic smectite precipitated during the hydrothermal alteration of bentonites (*e.g.*, Güven, 1974) or during early marine diagenesis (*e.g.*, Clauer *et al.*, 1990).

Furthermore, SAED patterns of smectite crystallites from the hypersaline mud flat samples have many discrete reflection spots representing multiple superimposed hexanets from larger coherent smectite domains than were observed in SAED patterns of smectite in the Inlet sample. The presence of such discrete diffraction spots from mud flat smectite is consistent with development of more highly ordered and coherent smectite packets than were observed in smectite from the Inlet sample. The development of coherent domains is consistent with precipitation of a discrete authigenic phase, or with precipitation of coherent authigenic overgrowths on original detrital Al-rich smectite.

The rapid disappearance of (00*l*) SAED patterns obtained from smectite crystallites from the Inlet sample is typical of rapid beam damage in highly disordered, small crystals. In contrast, (00*l*) SAED patterns of smectite from the hypersaline mud flat were more stable under the electron beam, compatible with the presence of larger, more coherent crystal domains in these samples. STEM and SAED textural and structural data are, therefore, collectively consistent with the presence of larger and more structurally coherent smectite crystallites in the hypersaline mud flat samples than in the marine Inlet sample, consistent with formation of authigenic smectite.

Mg-rich trioctahedral component

The trend of increasing Mg-enrichment in smectite from beidillitic compositions, typical of the marine Inlet sample, to saponitic compositions, typical of the hypersaline mud flat samples of the Salina Ometepec (Tables 2 and 3; Figure 8), provides the most compelling evidence for formation of authigenic smectite during early near-surface diagenesis. The Inlet smectite is dominantly dioctahedral; whereas the hypersaline mud flat sample is dominantly trioctahedral. Smectite compositions from different sites within the mud flat (*e.g.*, salina, Site 1 *vs.* sabkha mud flat, Site 3) or from different depths within the same site, widely overlap in Mg/Al ratios (Figure 8). These data suggest that whereas high Mg contents are unique to smectite in the hypersaline environment, they are not a strict function of burial depth (time in the mud flat) or geochemical environment of deposition (*e.g.*, salina *vs.* sabkha).

The data also indicate that smectite is variable in composition, consistent with a lack of equilibrium. Similar trends in Al:Mg:Fe and Al:Mg:K compositions and degree of heterogeneity were also obtained in smectite from diagenetically altered hypersaline Lake Abert sediments by Banfield *et al.* (1991b). To explain the heterogeneity, Banfield *et al.* (1991b) suggested that authigenic Mg-smectite with a composition close to stevensite precipitated on existing Al-rich, dioctahedral smectite particles. A similar mechanism may produce the heterogeneity in the smectites from the Salina Ometepec. Here, precipitation of Mg-rich trioctahedral saponitic smectite on original detrital dioctahedral smectite could explain the wide range in Mg/Al ratios and the apparent complex solid solution of both di- and trioctahedral components. Neoformation of separate Mg-rich saponite directly from sediment pore waters is compatible with the most Mg-rich smectite compositions.

K^+ as dominant interlayer cation

All AEM analyses of smectite from both the marine Inlet and the hypersaline mud flat contain K as the dominant interlayer cation (Tables 2 and 3). The high-K compositions cannot be explained by accidental inclusion of illite during analyses for two reasons. First, all reported compositions were either obtained on small individual crystallites in ion milled samples isolated from other grains (Figures 6B and 8C), or from the very outer edge of aggregate grains in grain mount samples (Figures 4 and 6). The analyzed areas had SAED patterns typical of smectite. Second, in the ion-milled samples, analyses were obtained only from crystallites with wavy, irregular lattice fringes with >10-Å spacing typical of smectite and SAED patterns showing disordered turbostratic stacking (*e.g.*, Figure 7B). Such smectite grains were distinguished readily from detrital illite or weathered micas, which occurred as larger grains, had very straight lattice fringes with 10-Å spacings (*e.g.*, Figure 7A), SAED patterns with evidence of some 2*M* polytypism (not shown), and compositions which were more Al and K-rich than associated smectites.

https://doi.org/10.1346/CCMN.1999.0470302 Published online by Cambridge University Press

The occurrence of K^+-rich smectite in hypersaline environments may not be unusual. Banfield *et al.* (1991b) also reported K^+ as the dominant interlayer cation in the authigenic stevensite precipitating in the hypersaline playa Lake Abert sediments. They furthermore suggested that the earlier interpretation of Jones and Weir (1983) of illite formation depleting K^+ in lake waters was explained better by the formation of K^+- and Mg^{2+}-rich smectite. Jones and Spencer (1985) also concluded that authigenic K^+ and Mg^{2+}-rich smectite (not illite) precipitated from hypersaline Great Salt Lake waters. Together, these data suggest that the presence of K^+ as the dominant interlayer cation in smectite is common in hypersaline environments. Other STEM and AEM studies investigating smectite compositions also show K^+ to be the dominant interlayer cation in smectite forming in normal marine environments (*e.g.,* Buatier *et al.*, 1989, 1992; Masuda *et al.*, 1992; Shau and Peacor, 1992).

IMPLICATIONS FOR BURIAL DIAGENESIS: HOW IMPORTANT IS EARLY DIAGENETIC Mg-SMECTITE?

The Mg-rich trioctahedral mixed-layer smectite-chlorite, corrensite, and chlorite clay mineral assemblages, commonly observed in sediments, are interpreted as forming in ancient hypersaline marine or lacustrine environments (Droste, 1963; Dyni, 1976; Bodine and Standaert, 1977; Tettenhorst and Moore, 1978; Eberl *et al.*, 1982; Khoury *et al.*, 1982; Bodine, 1985; Bodine and Madsen, 1987; Fisher, 1988; Turner and Fishman, 1991; Andreason, 1992; Hillier, 1993). Such Mg-rich assemblages were attributed to initial formation of mixed-layer trioctahedral corrensite or chlorite soon after deposition in hypersaline sediments by either neoformation or transformation of detrital minerals (*e.g.,* Turner and Fishman, 1991; Hillier, 1993 and references therein). However, there is *no* direct evidence from modern evaporative settings for early precipitation of corrensite or chlorite (*e.g.*, Bodine and Madsen, 1987). Instead, Bodine and Madsen (1987) proposed that mixed-layer smectite with chlorite-, corrensite-, and chlorite-bearing assemblages, common in ancient marine evaporites, are likely the result of burial diagenesis of Mg-rich trioctahedral smectite originally formed in the depositional environment by alteration of Al-rich dioctahedral smectite. They showed that at Mg^{2+} and H^+ ion activities typical of halite-saturated marine brines, dioctahedral Al-smectite plus dissolved Mg^{2+}, and H_4SiO_4 could react to form authigenic trioctahedral Mg-smectite of saponitic composition. Bodine and Madsen (1987) postulated that such Mg-rich smectite formed in the hypersaline depositional environment would react to form trioctahedral mixed-layer smectite-corrensite-chlorite assemblages during subsequent burial diagenesis, analogous to the reaction of smectite to mixed-layer illite-smectite to illite common during burial diagenesis of marine sediments. However, no modern marine depositional or diagenetic environment had been described in which such a dioctahedral smectite-to-trioctahedral smectite reaction occurred (Bodine and Madsen (1987).

The smectite diagenesis documented here from the Salina Ometepec provides a viable modern geochemical analog for a smectite-to-smectite reaction as postulated by Bodine and Madsen (1987). Solid-phase composition, together with water geochemical evidence, demonstrate that the formation of a K^+- and Mg^{2+}-rich saponitic smectite occurs near the sediment water interface during very early stages of diagenesis. The evidence further suggests that the trioctahedral smectite is formed at the expense of original detrital dioctahedral smectite. Similar conclusions were reached by Banfield *et al.* (1991b) for the formation of K^+-rich stevensite from aluminous dioctahedral smectite in the modern hypersaline Lake Abert. Hypersaline marine waters that have undergone gypsum precipitation are low in SO_4^{2-} content, as are most hypersaline lacustrine surface waters. The removal of SO_4^{2-} increases the activity of Mg^{2+} relative to normal seawater and could promote the precipitation of Mg-rich smectite. These relations imply that previous interpretations calling for illitization of smectite (*e.g.*, Stoffers and Singer, 1979; Singer and Stoffers, 1980), or formation of interlayer illite-chlorite (*e.g.*, Jones and Weir, 1983), must be reconsidered (*e.g.*, Banfield *et al.*, 1991b) given the increasing strength of geochemical evidence for the early diagenetic dioctahedral smectite-to-trioctahedral smectite reaction.

ACKNOWLEDGMENTS

J.R. Hansen, T.J. Huston, and D. Robinson are thanked for their invaluable help in the field and lab. C. Henderson, W.-T. Jiang and G. Li provided training on the SEM and STEM. B. McKee (Louisiana Marine Consortium) is thanked for providing ^{210}Pb analyses of sediment samples reported in Martini (1997). The manuscript was improved by thoughtful reviews by B. Jones, an anonymous reviewer, and the associate editor. Field work and sediment pore water analytical costs were partly funded by GSA research grants to A.M. Martini during 1993 and 1994. Additional funding was provided by PRF grant 27443-AC8 to L.M. Walter and by NSF grant EAR-9104565 to D.R. Peacor. The STEM used in this study was acquired under NSF grant EAR-87-08276. Electron microbeam analyses were partly supported by the Robert E. Mitchell Fund, University of Michigan.

REFERENCES

Ahn, J.H. and Peacor, D.R. (1989) Illite/smectite from Gulf Coast shales: A reappraisal of transmission electron microscope images. *Clays and Clay Minerals*, **37,** 542–546.

Ataman, G. and Baysal, O. (1978) Clay mineralogy of Turkish borate deposits. *Chemical Geology*, **22,** 233–247.

Andreason, M.W. (1992) Coastal siliciclastic sabkhas and related evaporative environments of the Permian Yates Formation, North Ward-Estes Field, Ward County, Texas.

American Association of Petroleum Geologists Bulletin, **76,** 1735–1759.

Baba, J., Peterson, C.D., and Schrader, H.J. (1991a) Modern fine-grained sediments in the Gulf of California. In *The Gulf and Peninsular Province of the Californias*, J.P. Dauphin and B.R.T. Simoneit, eds., Memoir 47, American Association of Petroleum Geologists, Tulsa, Oklahoma, 569–587.

Baba, J., Peterson, C.D., and Schrader, H.J. (1991b) Fine-grained terrigenous sediment supply and dispersal in the Gulf of California during the last century. In *The Gulf and Peninsular Province of the Californias*, J.P. Dauphin and B.R.T. Simoneit, eds., Memoir 47, American Association of Petroleum Geologists, Tulsa, Oklahoma, 589–602.

Bailey, S.W. (1988) X-ray diffraction identification of the polytypes of mica, serpentine and chlorite. *Clays and Clay Minerals*, **36,** 193–213.

Banfield, J.F., Jones, B.F., and Veblen, D.R. (1991a) An AEM-TEM study of weathering and diagenesis, Abert Lake, Orgeon: I. Weathering reactions in the volcanics. *Geochimica et Cosmochimica Acta*, **55,** 2781–2793.

Banfield, J.F., Jones, B.F., and Veblen, D.R. (1991b) An AEM-TEM study of weathering and diagenesis, Abert Lake, Oregon: II. Diagenetic modification of the sedimentary assemblage. *Geochimica et Cosmochimica Acta*, **55,** 2795–2810.

Berner, R.A. (1984) Sedimentary pyrite formation: An update. *Geochimica et Cosmochimica Acta*, **48,** 605–615.

Bodine, M.W., Jr. (1985) Trioctahedral clay mineral assembleges in Paleozoic marine evaporite rocks. In *Sixth International Symposium on Salt*, Northern Ohio Geological Society, 267–284.

Bodine, M.W., Jr. and Madsen, B.M. (1987) Mixed-layer chlorite/smectites from a Pennsylvanian evaporite cycle, Grand County, Utah. In *Proceedings of the International Clay Conference, Denver, 1985*, L.G. Schultz, H. van Olphen, and F.A. Mumpton, eds., The Clay Minerals Society, Bloomington, Indiana, 85–93.

Bodine, M.W., Jr. and Standaert, R.R. (1977) Chlorite and illite compositions from Upper Silurian rock salts, Retsof, New York. *Clays and Clay Minerals*, **25,** 57–71.

Brindley, G.W. (1955) Stevensite, a montmorillonite-type mineral showing mixed-layer characteristics. *American Mineralogist,* **40,** 239–247.

Buatier, M., Honnorez, J., and Ehret, G. (1989) Fe-smectite-glauconite transition in hydrothermal green clays from the Galapagos spreading center. *Clays and Clay Minerals*, **37,** 532–541.

Buatier, M.D., Peacor, D.R., and O'Neil, J.R. (1992) Smectite-illite transition in Barbados accretionary wedge sediments: TEM and AEM evidence for dissolution/crystallization at low temperature. *Clays and Clay Minerals*, **40,** 65–80.

Butler, G.P. (1969) Modern evaporite deposition and geochemistry of coexisting brines, the sabkha, Trucial Coast, Arabian Gulf. *Journal of Sedimentary Petrology*, **39,** 70–89.

Carpenter, A.B. (1978) Origin and chemical evolution of brines in sedimentary basins. *Oklahoma Geologic Survey Circular*, **79,** 60–77.

Clauer, N., O'Neil, J.R., Bonnot-Courtosi, C., and Holtzapffel, T. (1990) Morphological, chemical and isotopic evidence for an early diagenetic evolution of detrital smectite in marine sediments. *Clays and Clay Minerals*, **38,** 33–46.

Dong, H. and Peacor, D.R. (1996) TEM observations of coherent stacking relations in smectite, I/S and illite of shales: Evidence for MacEwan crystallites and dominance of $2M_1$ polytypism. *Clays and Clay Minerals*, **44,** 257–275.

Drever, J.I. (1971) Magnesium-iron replacement in clay minerals in anoxic marine sediments. *Science*, **172,** 1334–1336.

Drever, J.I. (1973) The preparation of oriented clay mineral specimens for X-ray diffraction analysis by a filter-membrane peel technique. *American Mineralogist*, **58,** 553–554.

Droste, J.B. (1963) Clay mineral composition of evaporite sequences. In *Symposium on Salt*, Northern Ohio Geologic Society, 47–54.

Dyni, J.R. (1976) Trioctahedral smectite in the Green River Formation, Duchesne County, Utah. *US Geologic Survey Professional Paper 967*, 14 pp.

Eberl, D.D., Jones, B.F., and Khoury, H.N. (1982) Mixed-layer kerolite/stevensite from the Amargosa Desert, Nevada. *Clays and Clay Minerals*, **30,** 321–326.

Eugster, H.P. and Hardie, L.A. (1978) Saline Lakes. In *Lakes, Chemistry, Geology, Physics*, A. Lerman, ed., Springer-Verlag, New York, 237–293.

Eugster, H.P. and Jones, B.F. (1979) Behavior of major solutes during closed-basin brine evolution. *American Journal of Science*, **279,** 609–631.

Fisher, R.S. (1988) Clay minerals in evaporite host rocks, Palo Duro Basin, Texas Panhandle. *Journal of Sedimentary Petrology*, **58,** 836–844.

Gac, J.Y., Droubi, A., Fritz, B., and Tardy, Y. (1977) Geochemical behavior of silica and magnesium during the evaporation of waters in Chad. *Chemical Geology*, **19,** 215–228.

Grim, R.E., Dietz, R.S., and Bradley, W.F. (1949) Clay mineral composition of some sediments from the Pacific Ocean off the California coast and the Gulf of California. *Geological Society of America Bulletin*, **60,** 1785–1808.

Güven, N. (1974) Lath-shaped units in fine-grained micas and smectites. *Clays and Clay Minerals*, **22,** 385–390.

Hansen, J.R., Hover, V.C., Walter, L.M., Lyons, T.W., Martini, A.M., and Robinson, D.M. (1993) Early siliciclastic diagenesis in an evaportive setting: Implications for C-S-Fe systematics and water/rock interactions. *Geological Society of America Abstracts with Programs*, **25,** 317–318.

Hillier, S. (1993) Origin, diagenesis, and mineralogy of chlorite minerals in Devonian Lacustrine mudrocks, Orcadian Basin, Scotland. *Clays and Clay Minerals*, **41,** 240–259.

Holser, W.T. (1979) Mineralogy of evaporites. In *Marine Minerals, Short Course Notes, Volume 6*, R.G. Burns, ed., Mineralogical Society of America, Washington, D.C., 211–294.

Humphreys, E.D. and Weldon, R.J., II (1991) Kinematic constraints on the rifting of Baja California. In *The Gulf and Peninsular Province of the Californias*, J.P. Dauphin and B.R.T. Simoneit, eds., Memoir 47, American Association of Petroleum Geologists, Tulsa, Oklahoma, 217–229.

Jackson, M.L. (1969) *Soil Chemical Analysis—Advanced Course*. By author, Madison, Wisconsin 895 pp.

Jiang, W.-T., Essene, E.J., and Peacor, D.R. (1990a) Transmission and analytical electron microscopic study of coexisting pyrophyllite and muscovite: Direct evidence for the metastability of illite. *Clays and Clay Minerals*, **38,** 225–240.

Jiang, W.-T., Peacor, D.R., Merriman, R.J., and Roberts, B. (1990b) Transmission and analytical electron microscopic study of mixed-layer illite/smectite formed as an apparent replacement product of diagenetic illite. *Clays and Clay Minerals*, **38,** 449–468.

Jones, B.F. and Weir, A.H. (1983) Clay minerals of Lake Abert, an alkaline, saline lake. *Clays and Clay Minerals*, **31,** 161–172.

Jones, B.F. and Spencer, R.J. (1985) Clay minerals in the Great Salt Lake basin. *Programs and Abstract, 1985 International Clay Conference*, Denver, Colorado 114 pp.

Khoury, H.N., Ebelr, D.D., and Jones B.F. (1982) Origin of magnesium clays from the Amargosa Desert, Nevada. *Clays and Clay Minerals*, **30,** 327–336.

Kim, J.-W., Peacor, D.R., Tessier, D., and Elsass, F. (1995) A technique for maintaining texture and permanent expansion of smectite interlayers for TEM observations. *Clays and Clay Minerals*, **43,** 51–57.

Kinsman, D.J.J. (1969) Modes of formation, sedimentary associations, and diagnostic features of shallow-water and supratidal evaporites. *American Association of Petroleum Geologists Bulletin*, **53,** 830–840.

Larson, R.L., Menard, H.W., and Smith, S.M. (1968) Gulf of California: A result of ocean floor spreading and transform faulting. *Science*, **161,** 781–784.

Lorimer, G.W. and Cliff, G. (1976) Analytical electron microscopy of mineral. In *Electron Microscopy in Mineralogy*, H.R. Wenk, ed., Springer-Verlag, New York, 506–519.

Martini, A.M. (1997) Hydrochemistry of saline fluids and associated water and gas. Ph.D. thesis, University of Michigan.

Martini, A.M. and Walter, L.M. (1993) Recent brines for the Salina Ometepec, Baja California: Chemical evolution of marine brines from a siliciclastic/evaporite environment. *Geological Society of America Abstracts with Programs*, **25,** 254.

Masuda, H., Tanaka, H., Gamo, T., O'Neil, J.R., Peacor, D.R., and Jiang, W.-T. (1992) Formation of authigenic smectite and zeolite and associated major element behavior during early diagenesis of volcanic ash in the Nankai Trough, Japan, ODP Leg 131. In *Water-Rock Interaction*, Y.K. Kharaka and A.S. Maest, eds., Balkema, Rotterdam, 1659–1662.

McCaffrey, M.A., Lazar, B., and Holland, H.D. (1987) The evaporation path of seawater and the coprecipitation of Br^- and K^+ with halite. *Journal of Sedimentary Petrology*, **57,** 928–937.

Merriam, R. and Bandy, O.L. (1965) Source of upper Cenozoic sediments in Colorado Delta region. *Journal of Sedimentary Petrology*, **35,** 911–916.

Millero, F.J. (1974) The physical chemistry of seawater. *Annual Review in Earth and Planetary Sciences*, **2,** 101–150.

Moore, D.M. and Reynolds, R.C., Jr. (1997) *X-ray Diffraction and the Identification and Analysis of Clay Minerals*, 2nd edition. Oxford University Press, Oxford, 332 pp.

Ortlieb, L. (1991) Quaternary vertical movements along the coasts of Baja California and Sonora. In *The Gulf and Peninsular Province of the Californias*, J.P. Dauphin and B.R.T. Simoneit, eds., Memoir 47, American Association of Petroleum Geologists, Tulsa, Oklahoma, 447–480.

Peacor, D.R. (1992) Diagenesis and low grade metamorphism of shales and slates. In *Minerals and Reactions at the Atomic Scale: Transmission Electron Microscopy, Reviews in Mineralogy, 27*, P.R. Buseck, ed., Mineralogical Society of America, Washington, D.C. 335–380.

Reynolds, R.C., Jr. (1980) Interstratified clay minerals. In *Crystal Structures of Clay Minerals and Their X-ray Identification*, G.W. Brindley and G. Brown, eds., Mineralogical Society, London, 249–303.

Sawlan, M.G. (1991) Magmatic evolution of the Gulf of California Rift. In *The Gulf and Peninsular Province of the Californias*, J.P. Dauphin and B.R.T. Simoneit, eds., Memoir 47, American Association of Petroleum Geologists, Tulsa, Oklahoma, 301–369.

Seidell, B.C. (1984) The anatomy of a modern marine siliciclastic sabkha in a rift valley setting: Northwest Gulf of California tidal flats, Baja California, Mexico. Ph.D. thesis, Johns Hopkins University, Baltimore, Maryland, 387 pp.

Shau, Y-H. and Peacor, D.R. (1992) Phyllosilicates in hydrothermally altered basalts from DSDP hole 504B, Leg 83—A TEM and AEM study. *Contributions to Mineralogy and Petrology*, **112,** 119–133.

Shearman, D.J. (1970) Recent halite rock, Baja California. *Institute of Mining and Metallurgy Transactions*, **79,** 155–162.

Singer, A. and Stoffers, P. (1980) Clay mineral diagenesis in two East African lake sediments. *Clay Minerals*, **5,** 291–307.

Stoffers, P. and Singer, A. (1979) Clay minerals in Lake Mobuto Sese Seko (Lake Albert)—Their diagenetic changes as indicator of the paleoclimate. *Geologische Rundschau*, **68,** 1009–1024.

Suarez-Vidal, F., Armijo, R., Morgan, G., Bodin, P., and Gastil, R.G. (1991) Framework of recent and active faulting in northern Baja California. In *The Gulf and Peninsular Province of the Californias*, J.P. Dauphin and B.R.T. Simoneit, eds., Memoir 47, American Association of Petroleum Geologists, Tulsa, Oklahoma, 285–300.

Tardy, Y., Cheverry, C., and Fritz, B. (1974) Néoformation d'une argile magnésienne dan les dépressions interdunaires du lac Tchad: Application aux domaines de stabilité des phyllosilicates alumineaux mangésiens et ferriéres. *Comptes Rendue de l'Academie Sciences Paris Serie C*, **278,** 1999–2002.

Tettenhorst, R. and Moore, G.E., Jr. (1978) Stevensite oolites from the Green River Formation of Central Utah. *Journal of Sedimentary Petrology*, **48,** 587–594.

Thompson, R.W. (1968) Tidal flat sedimentation on the Colorado River delta, northwestern Gulf of California. *Geological Society of America Memoir 107*, Geological Society of America, Boulder, Colorado, 133 pp.

Turner, C.E. and Fishman, N.S. (1991) Jurassic Lake T'oo'dichi': A large alkaline, saline lake, Morrison Formation, eastern Colorado Plateau. *Geological Society of America Bulletin*, **103,** 538–558.

van der Pluijm, B.A., Lee, J.H., and Peacor, D.R. (1988) Analytical electron microscopy and the problem of potassium diffusion. *Clays and Clay Minerals*, **36,** 498–504.

Veblen, D.R., Guthrie, G.D., Livi, K.J.T., and Reynolds, R.C., Jr. (1990) High-resolution transmission electron microscopy and electron diffraction of mixed-layer illite/smectite: Experimental results. *Clays and Clay Minerals*, **38,** 1–13.

Vonder Haar, S.P. and Gorsline, D.S. (1975) Flooding frequency of hypersaline coastal environments determined by orbital imagery: Geologic implications. *Science*, **90,** 147–149.

Walker, T.R. and Thompson, R.W. (1968) Late Quaternary geology of the San Felipe area, Baja California, Mexico. *Geology*, **76,** 479–485.

Walter, L.M., Bishof, S.A., Patterson, W.P., and Lyons, T.W. (1993) Dissolution and recrystallization in modern shelf carbonates: Evidence from pore water and sold phase chemistry. *Philosophical Transactions of the Royal Society (London)*, **A 344,** 27–36.

Walter, L.M. and Burton, E.A. (1990) Dissolution of recent platform carbonate sediments in marine pore waters. *American Journal of Science*, **290,** 601–643.

(Received 4 August 1997; accepted 15 September 1998; Ms. 97-069)